Article

A novel mechanobiological model of bone metastasis reveals that mechanical stimulation inhibits the pro-osteoclastogenic effects of breast cancer cells

Vatsal Kumar[1#], Syeda M. Naqvi[1#], Anneke Verbruggen[1], Eoin McEvoy[2] and Laoise M. McNamara[1*]

[1] Mechanobiology and Medical Device Research Group (MMDRG), University of Galway, Ireland.
[2] Biomedical Engineering, College of Science and Engineering, University of Galway, Ireland
[#] Both authors contributed to this manuscript equally
[*] Corresponding Author

Abstract: Tumor invasion into bone tissue during metastasis alters the biomechanical cues experienced by both tumor and native bone cells. These cues may drive bone lysis and tumor growth, yet how these govern tumor cell proliferation and the mechanobiological role bone cells (osteoblasts, osteoclasts and osteocytes) play in tumor invasion are not yet fully understood. Here, three-dimensional (3D) *in vitro* co-culture and computational models were first developed to investigate the coupled influence of tumor cell-bone cell signaling and growth induced matrix stress on tumor spheroid evolution. We next developed advanced *in vitro* engineered 3D models to mimic the complex *in vivo* multicellular and mechanical environments and confirmed the ability to recapitulate osteoblast, osteoclast and metastatic activity. We applied these models to study the development of osteolytic bone metastasis, in particular to investigate how interactions between tumor/bone cells and their surrounding environment dictate tumor invasion. Our results revealed that tumor spheroid growth is regulated by the synergistic influence of bone cell signaling and microenvironment stiffness. We also demonstrate for the first time in an *in vitro* 3D model of bone metastasis that the breast cancer cell driven pro-osteoclastogenic effects, which can facilitate cancer metastasis, is inhibited by mechanical compression.

1. Introduction

Bone metastasis occurs when primary tumor cells spread from their site of origin and invade bone tissue, where they form osteolytic or osteoblastic lesions[1]. Breast cancer highly targets bone tissue and it has been shown that osteoblasts express chemokines (CXCL12/SDF-1α), which facilitate homing of tumor cells to bone[2]. During osteolytic metastasis, tumor cells produce factors (parathyroid hormone-related protein (PTHrP), matrix metallopeptidases (MMPs), interleukins (IL-6, IL-8, IL-11) and/or vascular endothelial growth factor (VEGF)) that stimulate osteoclasts to actively degrade bone matrix[3] whereas osteoblasts to secrete RANKL, which further stimulates osteoclast resorption of bone matrix. This resorption results in a release of growth factors stored in the mineralized matrix, such as transforming growth factor β (TGF-β) or Insulin-like growth factors (IGFs), which stimulate tumor cell proliferation and further release of growth factors and thereby perpetuate tumor growth[3]. In this way, tumor cells and bone cells within bone tissue interact to enable tumor invasion as part of a complex process known as the 'vicious cycle'[4,5]. Although much research has been conducted to understand the pathogenesis of metastatic bone disease, it remains that therapies are deficient and once cancer invades bone tissue the condition is widely untreatable and accounts for 90% of cancer deaths worldwide[6]. Thus, there is a distinct need to significantly advance our scientific understanding of bone metastasis.

Many cells are intricately governed by the mechanical stimuli arising in their environment. Within bone, the coordinated activities of osteocytes, osteoblasts and osteoclasts govern structure and composition and elicit biochemical signaling to other cells (mechanotransduction) when this environment is not favorable. Mechanobiological factors have been implicated in breast cancer, in particular tumor growth, invasion, homing and metastasis[7-14]. Within the primary tumor, changes in the composition of the extracellular matrix occur, which alter the biophysical environment[15]. Such changes in mechanobiological cues contribute to growth and metastasis of breast cancer by promoting cell proliferation and transition of tumor cells to migrating cells[10-12,16-20]. Indeed, it has been demonstrated that MDA-MB-231 breast cancer cells (CC) cultured on stiff substrates (3 kPa) increased proliferation compared to those cultured on soft substrates (0.6 kPa) [21]. Furthermore, PTHrP expression is upregulated by MDA-MB-231 breast CCs with increasing substrate rigidity (2000 to 365,000 kPa), promoting the progression of the tumor cells from the pre-osteolytic to the osteolytic phase and formation of bone metastasis [22]. As they evolve, metastatic bone tumors become less stiff compared to non-tumor bone tissue [23,24] and the presence of the tumor might alter the biophysical cues acting on bone cells. Given the well-established relationship between matrix properties, mechanical stimuli and bone biology, such changes may activate mechanobiological responses in both tumor cells and native bone cells, perpetuating the "vicious cycle", and ultimately leading to bone lysis and tumor growth. However, how the coupled mechanobiological responses of tumor and bone cells contributes to osteolysis and tumor growth is not understood.

Much of our understanding of metastasis comes from animal models [25-30], in which the normal responses of the immune system are suppressed, or *in vitro* cell culture studies that are conducted using 2D multi-well plates, which do not represent the complex *in vivo* environment due to the loss of native morphology and interactions with the surrounding matrix[31]. More recently, three-dimensional (3D) *in vitro* tumor models have been developed to study the invasion of breast CCs in the presence of multiple bone cell types by co-culturing the breast CCs with bone specimen collected from patients undergoing total hip replacement[32,33]. These studies showed the specificity of breast and prostate CCs towards metastasizing to bone as well as established 3D humanized in vitro models of bone to study differences in tumor colonization and proliferation between healthy and osteoporotic condition. A recent experimental model used bioprinted calcium phosphate coated polycaprolactone scaffolds cellularized with human osteoprogenitor cells, which were then seeded with human prostate CCs[34] to study response to androgen-targeted therapy. They reported that cancer/bone stroma interactions and anti-androgens drive cancer progression in a mineralized microenvironment. Another study fabricated a metastatic bone model by encapsulating osteoblasts, osteoclasts, bone-resident macrophages, endothelial cells and breast CCs in a fibrin hydrogel [35] and showed organ-tropism of breast CCs towards bone. By comparison with a simplified metastatic muscle model (myoblasts, fibroblasts, endothelial cells and breast CCs), the authors observed that the proliferation of breast CCs was significantly lower in the metastatic muscle model as shown by the analysis of the area fraction covered by CCs. Another study used a 3D printed scaffold,

made up of a biocompatible resin (DS3000) conditioned with osteoblast-like cells, a collagen matrix, and mineralized calcium to which patient-derived xenografted metastatic breast CCs were added [36]. They demonstrated that the metastatic breast CCs colonized the scaffold and exhibited a modulated sensitivity to chemotherapy drugs, similar to *in vivo* chemotherapy, where breast CCs are not completely eliminated by the treatment, in contrast to that observed under 2D conditions. A more recent study developed bone-like scaffolds using collagen matrices with controlled intrafibrillar mineral deposition and decellularized bone scaffolds with intact organic ECM configuration and microstructure and showed the importance of matrix mineralization in early stage bone metastasis[37]. Here they showed that higher levels of mineral led to quiescence through a reduction in mechanosignaling. More recently, a 3D *in vitro* tumor model was developed in our lab to study the invasion of breast CCs (4T1 murine mammary carcinoma cells) in isolation[38]. These cells were encapsulated in gelatin-transglutaminase (mtgase) hydrogels with varying substrate stiffness (1 or 2.7 kPa) to mimic the properties of bone marrow. To understand the influence of mechanical stimuli on tumor growth, the same study used a custom bioreactor to apply cyclic mechanical compression (1 hour/day for 4 days) and the proliferation of the 4T1 cells was studied[38]. The results revealed that tumor spheroid growth was restricted in stiffer and mechanically compressed hydrogels. Indeed, mechanical compression has been reported to inhibit tumor growth through reduced osteolysis in immunocompromised SCID mice, and *in vitro*, in poly(lactide-co-glycolide) (PLG) and hydroxyapatite (HA) scaffolds seeded with MDA-MB-231 cells[39]. Another work demonstrated that lower (1N) compressive loads had suppressive effects on tumor-induced osteolysis in a mouse model [40]. Advanced experimental models that can replicate both (1) the complex multicellular niche (osteoblasts, osteoclasts, osteocytes, tumor cells) and (2) the native mechanical environment are required to investigate how mechanical stimulation arising in the bone environment may regulate the development of osteolytic bone metastases.

The specific objectives of phase one of this research was to (1) study the growth-induced matrix stress on tumor spheroid evolution by developing a 3D in-vitro model and a novel computational tumor spheroid growth model using finite element modelling. The in-vitro model was then extended to include bone cells to (2) study the coupled influence of tumor cell-bone cell signaling on tumor spheroid evolution. Given the importance of a mineralized environment in early stage bone metastasis, the key objective of phase two of this research was to (3) advance the co-culture models developed in the earlier phase of this research. We did this by including the multicellular niche of osteoblasts and osteocytes within a mineralized matrix followed by co-culturing with osteoclasts and/or breast CCs and concurrently incorporating mechanical loading using a custom designed bioreactor to mimic the complex multicellular and mechanical environment *in vivo*. We applied this model to test the hypothesis that "mechanical compression will inhibit osteolytic activity within these mimetic models".

2. Results

2.1 Tumor spheroid growth is stress dependent

Multicellular spheroids are a promising experimental model for *in vivo* tumor growth, but the biomechanical factors regulating such growth in a three-dimensional (3D) environment remain unclear. To investigate the mechanoregulation of spheroid expansion, we encapsulated 4T1 breast cancer cells in a monoculture configuration within gelatin-transglutaminase hydrogels of varying compression modulus, reflective of the mechanical properties of bone marrow [41] (Figure 1a). We monitored spheroid development over 7 days, starting from single cells, and observed that the rate of spheroid growth reduced with increasing gel stiffness (Figure 1b). We hypothesized that the reduction in spheroid size was driven by reduced proliferation as opposed to cellular compaction induced by increased confinement. We thus characterized the number of cells per spheroid, and indeed found that the number of cells was higher in softer hydrogels (Figure 1b). To investigate whether cell proliferation was stress-dependent, we developed a computational model to characterize mechanosensitive growth. We considered that the proliferation of tumor cells (c_t) was dependent on spheroid stress ($\boldsymbol{\sigma}$) induced by hydrogel deformation, such that

$$\frac{\mathrm{dc_t}}{\mathrm{dt}} = \left(\frac{\mathrm{c_t}}{\tau_\mathrm{t}}\right)(1 - \mathrm{tr}(\boldsymbol{\sigma})/(3p_0)), \tag{1}$$

where τ_t is the timescale for tumor proliferation in the absence of other factors and p_0 is the reference pressure for mitotic inhibition. To simulate growth we adopted a multiplicative decomposition of the deformation gradient $\mathbf{F}$ into $\mathbf{F_g}$ (growth tensor) and $\mathbf{F_e}$ (elastic tensor)[42,43], such that $\mathbf{F} = \mathbf{F_e}\mathbf{F_g}$. Here, $\mathbf{F_g} = \lambda_g \mathbf{I}$, where $\lambda_g = (c_t/c_0)^{1/3}$ is the growth stretch, $\mathbf{I}$ is the second order identity tensor and c_0 is the initial number of cells in a spheroid. Simulations revealed that the increased circumferential and radial stresses generated by spheroid expansion in a stiffer microenvironment can reduce the rate of cell proliferation, in agreement with our experimental observations (Figure 1d-1e). Having established that 4T1 spheroid growth is stress-dependent, we proceeded to explore the coupled influence of hydrogel stiffness and bone cell signaling on *in vitro* tumor development.

2.2 Osteoclasts have an inhibitory effect on tumor spheroid growth which is partially alleviated by osteoblasts

To study the coupled effect of individual bone cells on tumor spheroid growth, RAW264.7 osteoclast precursors and MC3T3-E1 osteoblast-like cells were encapsulated within separate gelatin-transglutaminase hydrogel suspensions and cultured in different culture configurations with 4T1 cells for 7 days: mono-culture (4T1), co-culture (RAW264.7 + 4T1, MC3T3 + 4T1) and tri-culture (MC3T3 + RAW264.7 + 4T1 (Figure 2a).

When co-cultured with MC3T3 cells, the size of the 4T1 tumor spheroids was significantly lower relative to those that were formed in the 4T1 monoculture, only in the 0.58 kPa hydrogels. However, when co-cultured with RAW264.7 cells, the tumor spheroids were significantly smaller than the ones formed in monoculture in 0.58 kPa, 0.85 kPa and 1.1 kPa hydrogels. (Figure 2d). This reduction in spheroid size in co-culture with RAW264.7 cells was partially mitigated with the inclusion of MC3T3 cells (i.e. in the tri-culture group) in 0.58 and 0.85 kPa hydrogels (Figure 2d).

To further understand the biochemical signaling occurring between the 4T1, RAW264.7 and MC3T3 cells that may be causing the changes in tumor spheroid growth, we carried out Quantitative Real Time PCR (qRT-PCR) and looked at the mRNA expression of certain genes that are expressed by these cell types and that are implicated in the growth of tumor cells (TGF-β, TNF-α, IL-6 and PTHrP). Transforming growth factor beta (TGF-β) was downregulated, compared to the 4T1 monoculture, in tri-culture group (p=0.0599) and the RAW264.7 co-culture group (p=0.0557) in the 0.85 and 1.1 kPa hydrogels, respectively (Figure 2e). Tumor necrosis factor alpha (TNF-α) mRNA expression, when compared to the 4T1 monoculture, was upregulated in the RAW264.7 co-culture (p=0.0657) in the 0.58 kPa hydrogel and the tri-culture group in the 0.58 kPa (p=0.014) and 0.85 kPa (p=0.0469) hydrogels (Figure 2f). We observed lower expression of TNF-α in the MC3T3 co-culture group when compared to RAW264.7 co-culture (p=0.0081) and when compared to the tri-culture group (p=0.0012) in the 0.58 kPa hydrogels and tri-culture group in the 0.85 kPa hydrogel (p=0.016) (Figure 2f). We also looked at the mRNA expression of Interleukin 6 (IL-6) and observed that there was an upregulation in its expression, when compared to the 4T1 monoculture, in the MC3T3 co-culture group in the 0.85 kPa (p=0.0347) and 1.1 kPa (p=0.0337) hydrogels (Figure 2g). There was higher expression of IL-6 in the MC3T3 co-culture group when compared to RAW264.7 co-culture in the 0.58 kPa (p=0.0195), 0.85 kPa (p=0.0647) and 1.1 kPa (p=0.0181) hydrogels (Figure 2g). We then looked at the expression of PTHrP and observed that there was higher expression in the RAW264.7 co-culture group in the 1.1 kPa hydrogels when compared to the 0.58 kPa (p=0.0057) and 0.85 kPa (p=0.0812) hydrogels (Figure 2h). For the MC3T3 co-culture group, there was higher expression of PTHrP in the 1.1 kPa hydrogels when compared to 0.58 kPa (p=0.0790) and 0.85 kPa (p=0.0042) hydrogels (Figure 2h).

2.3 Development of a Bone Multicellular Model: presence of mineral deposits and active osteoclasts

While the findings above focus on mimicking the bone marrow biophysical environment, tumor cells also invade mineralized niches in the bone. A recent study showed the importance of mineralization when studying early stage metastases demonstrating that mineralization (1) alters breast cancer cell gene expression and growth in vitro (2) increases a stem-like phenotype in breast cancer cells and (3) regulates breast cancer cell phenotype by altering mechanosignaling[37]. *In vivo*, multiple bone cells reside within a 3D niche, where they interact biochemically and experience mechanical loads. Thus, to more closely mimic the *in vivo* physiological and mechanical environment, bone multicellular (BM) models were fabricated by (1) developing mineralized

hydrogels complete with OCY 454 and MC3T3-E1 cells within gelatin-mtgase hydrogels cultured in osteogenic media for 21 days, (2) layering murine RAW264.7 osteoclast precursor encapsulated gelatin-mtgase hydrogels onto these mineralized constructs and (3) subjecting these models to mechanical stimulation at 0.5% strain using a custom built compression bioreactor for 1 hour per day for 7 days (Figure 3a-3b, Figure 5a-5b). Constructs under static conditions served as controls.

The results from this study confirm the development of a mineralized 3D bone-multicellular model under both static and stimulated conditions, as confirmed by micro-CT scanning at both day 24 and day 28 (Figure 3c). Biochemical analyses reveal an increase in calcium content in the mechanically stimulated BM model compared to static controls at day 24, and no significant difference between stimulated and static groups at day 28 (Figure 3d). A significant decrease in calcium content was observed in the stimulated groups at day 28 compared to day 24. By micro-CT analysis, no change in mineral volume (BV/TV) was evident between static and stimulated groups at day 24 or day 28 (Figure 3e). However, by day 28, BM models had developed significantly more high-density mineral content (M_{high}) than at day 24, both in the static and stimulated groups (Figure 3f). Interestingly, under static conditions there is a significant increase in full width at half max (FWHM) at day 28 compared to day 24 (Figure 3g).

Quantitative real time PCR (qRT-PCR) revealed that mechanical stimulation upregulated osteogenic genes. Specifically, bone sialoprotein (BSP2 – intermediate osteoblast marker) mRNA expression was upregulated in mechanically stimulated groups compared to static controls at day 24 (Figure 3i). Osteopontin (OPN – early osteoblast marker) and dentin matrix acidic phosphoprotein 1 (DMP1 – late osteoblast marker) mRNA expression was upregulated in mechanically stimulated groups compared to static controls at day 28 (Figure 3h, 3j). Of note, BSP2 mRNA expression was downregulated in mechanically stimulated groups compared to static controls at day 28 (Figure 3i).

There was a significant increase in pro-osteoclastogenic gene expression (RANKL (receptor activator of NF-κβ ligand): OPG (Osteoprotegerin) ratio) in mechanically stimulated BM models at day 24 compared to static controls (Figure 3k). In contrast to day 24 results, there was a significant decrease in RANKL:OPG ratio in mechanically stimulated BM models at day 28 compared to static controls (Figure 3k). This in keeping with the known inhibitory effect of mechanical loading on bone resorption[44,45]

Immunofluorescence and histology for Cathepsin-K (CTSK), Tartrate Resistant Acid Phosphatase (TRAP) and Haemotoxylin and Eosin (H&E) confirmed the differentiation of osteoclast precursors to multinucleated active osteoclasts (nuclei > 3) (CTSK and TRAP positive) osteoclasts in the in mineralized bone-like multicellular 3D models (BM model) at both day 24 and day 28 under both mechanically stimulated and static conditions (Figure 3l). Nuclear Factor of Activated T Cells 1 (NFATC1) and Osteoclast-associated receptor (OSCAR) mRNA expression was significantly upregulated under mechanical stimulation in the BM model when compared to static controls and at day 28 (Figure 3m and 3n). There was no observed difference in IL-6 and Avβ3 immunofluorescence staining between the static and stimulated groups (Figure 3o).

2.4 Metastatic Multicellular model exhibit osteolytic metastatic response

To mimic the physiological and mechanical environment of bone metastasis *in vivo*, metastatic multicellular (MM) models were fabricated by layering murine RAW264.7 and 4T1 breast cancer cell encapsulated gelatin-transglutaminase onto previously mineralized hydrogels (approach described above) and were subjected to mechanical stimulation at 0.5% strain for 1 hour per day using a custom built compression bioreactor for 7 days (Figure 4a-4b, Figure 5a-5d). Constructs under static conditions served as controls. We confirmed cancerous behavior of the MM model based on increased cancer cell activity (PTHRP mRNA expression and IL-6 immunostaining). We also confirmed the metastatic behavior of the MM model based on reduced osteoblast activity, increased osteoclastogenesis and pro-osteoclastogenic gene expression.

Paracrine signaling for osteoclastogenesis (RANKL:OPG ratio) was significantly higher for the metastatic multicellular (MM) model(day 24:0.57 ± 0.05; day 28: 3.05 ± 0.14, respectively) compared to the BM model (day 24:0.03 ± 0.05; day 28:0.62 ± 0.05) under static conditions (Figure 3k, 4m and 5d). Moreover, mRNA expression of OSCAR was significantly upregulated in MM model (406.62 ± 10.54) at day 28 compared to BM model (4.39 ± 0.11) under static conditions (Figure 3n, 4o and 5d). Furthermore, IL-6 staining

and mRNA expression of PTHrP were notably increased in the MM model under static conditions (7.65 ± 0.41) at day 28, compared to the BM model (0.55 ± 0.46), see Figures 3o, 4l, 4o and 5d. These results are in keeping with the known osteolytic nature of 4T1 breast cancer cells and confirms the models ability to recapitulate the osteolytic metastatic process.

Under static conditions, there was significantly ($\rho < 0.05$) more high-density mineral in the MM models (MHigh 8.88 ± 0.102) compared to BM model (MHigh 0.3 ± 0.104) by day 24 but no significant difference by day 28 (Figure 3f,4g). Furthermore, static MM models (FWHM 426.36 ± 23.86) were significantly ($\rho < 0.05$) more heterogeneous at day 24 compared to static BM models (FWHM 172.52 ± 1.34), but not at day 28 (Figure 3g,4h). Mineral heterogeneity is an indicator of poor bone quality, and has been previously reported in osteolytic bone tissue from pre-clinical animal models of breast cancer metastasis[46,47] as well as in trabecular bone tissue in the femoral heads of osteoporotic and diabetic patients[48]. BSP2 mRNA expression was significantly downregulated in the presence of 4T1 breast cancer cells (1741.87 ± 80.92) compared to BM model (9703.13 ± 60.72) by day 28, suggesting reduced osteoblast activity in the MM model (Figure 3i, 4i and 5d).

2.5 Osteolytic metastatic response is attenuated under mechanical compression

Osteoclast marker OSCAR (Figure 4n) mRNA expression was significantly upregulated in the mechanically stimulated MM model at day 24 compared to static controls, however, there was a significant downregulation of OSCAR under stimulation at day 28 (Figure 4n, Figure 5e), when compared to static controls. Most interestingly, mechanical stimulation resulted in a reduction in RANKL/OPG expression in MM models at both day 24 and day 28 compared to static controls (Figure 4m, Figure 5e). Furthermore, mRNA expression of PTHrP and immunostaining for IL-6 were found to be significantly downregulated/decreased in the mechanically stimulated MM model compared to static control at day 28 (Figure 4l-4p, Figure 5e).

ALP activity increased in the mechanically stimulated MM models compared to the static controls at day 24 (Figure 4c). By day 28, there was no significant difference in ALP activity and calcium content between static and stimulated models (Figure 4d, 4e). MicroCT data indicated reduced bone-like mineral volume fraction in the mechanically stimulated MM models compared to the static controls at day 24 (Figure 4f). Mineral volume fraction was reduced by day 28 compared to day 24 in the static MM models. However, a significantly larger % of mineral was high in density (Mhigh) in the mechanically stimulated MM models, compared to MM static controls by day 28 (Figure 4g).

Quantitative RT-PCR indicated downregulation in BSP2 mRNA expression at day 24 and an upregulation at day 28 in the MM models in response to mechanical stimulation compared to static controls (Figure 4i, Figure 5e). DMP1 and SOST mRNA expressions were significantly upregulated in the mechanically stimulated MM model compared to static controls at both time points for DMP1 and at day 24 for SOST (Figure 4j-4k, Figure 5e). A similar upregulation in DMP1 mRNA expression was evident at day 28 (Figure 4j). However, SOST mRNA expression at day 28 was downregulated in response to mechanical stimulation compared to static controls (Figure 4k).

3. Discussion

Bone is subjected to unique physical and biomechanical conditions that are not easily replicated *in vitro*, but biomaterial-based organoid cultures are a step closer to achieving more accurate models for studying bone pathology. We firstly cultured 4T1 breast CCs within gelatin-mtgase hydrogels and investigated the influence of matrix stiffness on tumor spheroid growth. Simultaneously we developed a novel computational model to characterize the stress sensitivity of the growth of these tumor spheroids. Next, we co-cultured bone cells (MC3T3-E1, RAW264.7) with the 4T1 cells and investigated the coupled influence of matrix stiffness and tumor cell-bone cell signaling on tumor spheroid growth. Our results reveal for the first time a synergistic influence of osteoclasts, osteoblasts and 3D matrix stiffness on tumor spheroid growth. We further developed a 3D mineralized bone multicellular (BM) model and applied extrinsic mechanical compression using a custom-built compression bioreactor to recreate the multicellular and mechanical environment *in vivo*. Next, we developed a metastatic multicellular (MM) model, which recreated the typical pro-osteoclastogenic effect of

breast cancer cells under static conditions. Using this model, we were able to investigate how mechanical stimulation inhibited this pro-osteoclastogenic response. Altogether, this study provides advanced *in vitro* 3D multicellular experimental and computational models for studying the coupled influence of growth induced matrix stress and tumor cell-bone cell signaling on tumor spheroid growth during metastasis. The results of this study highlight the importance of mechanical loading in inhibiting osteoclastogenesis and its influence on breast cancer cell mediated reduction in mineral content in the early stage bone metastasis.

This study has a number of limitations that must be considered. Firstly, there are inherent limitations in using cell lines, which may respond differently to primary cells. Nonetheless, we incorporated a combination of cell lines from similar origins; our experiments used mouse bone cells and cancer cells, so the potential effects of cross-species interactions do not have to be taken into consideration. Another limitation is that the immune cells and endothelial cells were not included, which might better represent the *in vivo* environment. Thirdly, this study incorporated only compression stimulus, thereby not replicating other mechanical loading environments *in vivo* such as perfusion. However, the mechanical stimulus (0.5% compressive strain) was chosen to induce osteogenic differentiation[49] and so was important for the model development. Lastly, these models are not fully representative of *in vivo* bone in terms of the extent of mineral deposition and stiffness. The compression modulus of bone multicellular mineralized model after 28 days of culture (16.203 +/- 0.089 kPa) did not approach that of the bone (~0.5-25 GPa). However, it is important to note that the stiffness of our gels at day 0 was 0.58 kPa so relative to that, the stiffness of the mineralized 3D models in this study increased 27 fold.

Our computational model simulations and experimental analysis confirm that tumor cell proliferation is stress dependent, but more importantly we show for the first time that the co-culture of 4T1 cells with osteoblasts or osteoclast precursors further reduced tumor spheroid size. Significant reductions in tumor spheroid size in co-culture with osteoclast precursors could be attributed to the expression of TNF-α and TGF-β1, both factors known to be secreted by the RAW264.7 cells[50,51], which have previously been linked to reduced tumor growth [52-54]. Indeed, in this study we observe significant differences in TNF-α expression such that we have an upregulation in the osteoclast precursor co-culture and tri-culture groups only. Interestingly, we observed increases in tumor spheroid size when in co-culture with osteoblasts compared to RAW264.7 co-culture and tri-culture groups. Osteoblasts might regulate spheroid growth through their expression of IL-6, which has been shown to suppress osteoclastogenesis of precursor cells, which may in-turn affect production of TGF-β[55]. In this study we observed an upregulation of IL-6 in the osteoblast co-culture group compared to RAW264.7 co-culture and tri-culture groups.

This study confirms the development of a novel mineralized 3D bone-like multicellular model as evidenced by presence of calcium content, mineral volume and upregulation of osteoblast markers BSP and OPN. Despite an increase in calcium content in the mechanically stimulated bone-like model compared to static controls at day 24, calcium content appeared to be similar for bone-like models cultured with and without mechanical stimulation at day 28. This is in contrast to a previous study in our laboratory demonstrating that the application of mechanical stimulation resulted in increased mineralization in osteoblast-encapsulated hydrogels *in vitro*[56]. This suggests that in a multicellular configuration there is a suppression of the typical induction of mineral production by osteoblasts cultured in isolation under mechanical stimulation. In other studies, mechanical stimulation of osteoblasts has been shown to activate specific signaling pathways[57], which stimulate the production of anabolic growth factors and synthesis of extracellular matrix proteins and mineral[58]. In fact, dynamic compression can promote the differentiation and mineralization of both osteoblasts and stem cells toward osteogenesis both *in vitro* and *in vivo*[59-63]. It may be that the presence of osteoclasts inhibited mineral production by signaling to osteoblasts. Interestingly, semaphorin 4D produced by osteoclasts inhibits bone formation[64] in a manner similar to that of OPG, which limits the osteoclast-promoting actions of RANKL. In this study, OPG was significantly upregulated in the mechanically stimulated bone-like model compared to static controls. Another explanation may be that the active osteoclasts degraded the mineral in the timeframe of the study. Indeed, RANKL:OPG ratio and gene expression of osteoclast markers NFATC1 and OSCAR were significantly greater in mechanically stimulated bone-like groups compared to static.

The results from this study further confirm the development of a novel 3D bone metastatic-like model. PTHrP is a known growth factor secreted by tumor cells, that plays an important role in the 'vicious cycle' cascade of events by stimulating the expression of RANKL by osteoblasts and osteocytes leading to osteoclast formation and ultimately bone loss[65]. Moreover, IL6 has been shown to enhance osteoclastogenesis by upregulating RANKL in osteocytic MLO-Y4 cells[66]. We report that gene expression of PTHrP, osteoclast marker OSCAR and fluorescence intensity for IL-6 and CTSK were all upregulated or increased significantly for the bone metastatic-like model compared to the bone-like model under static conditions. These results are in keeping with the known osteolytic nature of 4T1 breast cancer cells and confirms the model's ability to recapitulate the osteolytic metastatic process [67]. Furthermore, these results confirm the differentiation of osteoclast precursors to active multinucleated osteoclasts in the metastatic model.

Mechanical stimulation reduced bone volume fraction, gene expression of PTHrP, pro-osteoclastogenic signaling (RANKL/OPG ratio) and IL-6 staining in the metastatic model when compared to static controls. It has been demonstrated that the anti-catabolic effects of mechanical loading are modulated by nitric oxide (NO). Mechanical stimulation stimulates the release of NO from bone cells [68,69], and NO induces a decrease in the RANKL/OPG ratio. Although active osteoclasts were present in the mechanically stimulated metastatic model, there was a significant downregulation of OSCAR at day 28, compared to static controls. These results confirm the differentiation of osteoclast precursors to multinucleated active osteoclasts in the mineralized multicellular 3D models. Of importance, addition of osteoclast precursors to the 3D mineralized model, induced their differentiation into osteoclasts in both the bone-like multicellular and metastatic models without the need of an externally added cytokine to stimulate osteoclastogenesis e.g. RANKL. In this way, we demonstrate the potential for these primed mineralized models (cultured in osteogenic growth factors) to be used in subsequent studies involving the use of osteoclast precursors.

4. Conclusions

This study provides an advanced understanding that tumor growth and osteolysis-mediated changes in matrix stiffness lead to an evolving mechanical environment during tumor invasion of the bone, which our results have shown can regulate both tumor cell and bone cell behavior. Using novel experimental and computational tumor growth models we showed for the first time, a synergistic influence of osteoclasts, osteoblasts and 3D matrix stiffness on tumor spheroid growth. Furthermore, we developed an advanced 3D *in vitro* model for studying bone biology and pathology, which represents (1) bone-like osteoblastic and osteoclastic activity and (2) early stage metastatic response to the addition of breast CCs. By developing this advanced biomimetic 3D *in vitro* mineralized bone multicellular model, we successfully captured the osteolytic-metastatic process. This study also reveals the importance of mechanical loading in attenuating osteoclastogenesis and its influence on breast cancer cells in early stage bone metastasis. This model will be used in the future to establish whether inhibition of mechanobiological responses can attenuate tumor cell-bone cell signaling and the development of osteolytic bone metastases.

5. Materials and Methods

5.1 Expansion of cells

Murine OCY454 osteocytic cells (Centre for Skeletal Research Bone Cell Core, an NIH-funded program (P30AR075042), which is supported by NIAMS) were expanded on type I collagen (0.15 mg/ml in 0.02 M acetic acid) coated T-175 flasks in standard growth media (α-MEM supplemented with 10% FBS, 100 U/mL penicillin, 100 μg/mL streptomycin and 2 mM L-glutamine) at the permissive temperature of 33°C in a humidified 5% CO_2 environment. The OCY454 cells were differentiated on T-175 flasks at the semi-permissive temperature of 37°C for 14 days in a humidified 5% CO_2 environment. Murine MC3T3-E1 osteoblastic cells (ATCC, Manassas, VA, USA) were expanded in standard growth media and maintained at 37°C in a humidified 5% CO_2 environment. Murine RAW264.7 osteoclast precursors (ATCC, Manassas, VA, USA) were expanded in their growth media (low glucose DMEM supplemented with 10% FBS (HyClone), 100 U/mL penicillin, 100 μg/mL streptomycin and 2 mM L-glutamine) and maintained at 37°C in a humidified 5% CO_2 environment. Murine mammary carcinoma 4T1 cells were expanded in their growth media (Roswell Park

Memorial Institute (RPMI) supplemented with 10% FBS, 100 U/mL penicillin and 100 μg/mL streptomycin) and maintained at 37°C in a humidified 5% CO_2 environment. Cell culture media was replenished every 3 days.

5.2 Three-dimensional (3D) Static Culture

Cell encapsulating gelatin hydrogels of 3 different stiffness (0.58 kPa, 0.85 kPa ,1.1 kPa) were developed by crosslinking equal volumes of 9% cell laden gelatin and nano-Hydroxyapatite (nHa) (5.5% v/v) with sterile microbial transglutaminase (mtgase) containing Activa WM (Aginomoto Foods) of different concentrations (0.3%, 0.6%, 1% w/w). These hydrogels had 4T1 breast CCs, MC3T3-E1 osteoblast-like cells, and RAW264.7 osteoclast-precursors in separate layers in various culture configurations (Monoculture:4T1, Co-culture: RAW+4T1, MC3T3+4T1, Tri-culture: MC3T3+RAW+4T1). The cell number was kept at 100,000 cells/hydrogel layer (2×10^6 cells/mL of hydrogel). All groups were cultured for 7 days (Fig. 1A) and assessed for tumor spheroid size (Actin, Nucleus), cell number (DNA) and proteins implicated in tumor cell- bone cell signaling: PTHrP, IL-6, TGF-β and TNF-α.

5.3 Fabrication of Bilayered models for mineralization

OCY454 cells were suspended in gelatin with an initial concentration of 9%. This cell suspension was enzymatically cross-linked with mtgase and with nHA (1:1:1 ratio), to yield a final gelatin concentration of 3% w/v, a mtgase concentration of 0.3% w/w of gelatin, a nHA concentration of 5.5% v/v, and an OCY454 cell density of 2×10^6 cells/mL. To fabricate the OCY454 layer this suspension was then pipetted into custom-made polydimethylsiloxane (PDMS) wells (1.33 mm × 6 mm D × 13 mm) and allowed to cool at 4°C for 8 min. Next, an MC3T3 gelatin/nHA suspension was crosslinked with mtgase as described for OCY454 cells. This suspension was pipetted on top of the OCY454 layer and allowed to cool at 4°C for 8 min to form an osteoblast layer (1.33 mm × 6 mm D × 13 mm). These bilayered models were cultured in standard growth media (α-MEM, 10% FBS, 100 U/mL penicillin, 100 μg/mL streptomycin, 2 mM L-glutamine) supplemented with osteogenic factors (50 μM ascorbic acid, 10 mM β-glycerophosphate, and 100 nM dexamethasone). Media was replenished every 3 days during a culture period of 21 days to allow for mineralization to occur.

5.4 Fabrication of bone multicellular (BM) and metastatic multicellular (MM) models

To fabricate the bone multicellular (BM) model, RAW264.7 encapsulated gelatin/nHA was enzymatically cross-linked with mtgase as described earlier. This suspension was pipetted on top of the osteoblast layer of the bilayered models, which had been cultured for 21 days as described in 2.2 above. These were allowed to cool at 4°C for 8 min.

To fabricate the metastatic multicellular (MM) model, RAW264.7 and 4T1 (1:1) encapsulated gelatin/nHA was enzymatically cross-linked with mtgase as described earlier. This suspension was pipetted on top of the osteoblast layer of the bilayered models. These were allowed to cool at 4°C for 8 min. These models were cultured as follows: (1) Bone Multicellular (BM): RAW 264.7 growth media and MC3T3/OCY454 growth media mixed at a ratio of 1:2 or (2) Metastatic Multicellular (MM): RAW 264.7 growth media, 4T1 growth media and MC3T3/OCY454 growth media mixed in a ratio of 1:1:2. Media was replenished every 3 days for the culture period to allow for proliferation and differentiation of the pre-osteoclasts and adenocarcinoma cells (7 days).

5.5 Mechanical Stimulation

Models from each experimental group were transferred from well plates to a sterile custom bioreactor (VizStim) containing their respective media, as described above. Four models were placed within each bioreactor chamber. The models were subjected to compression at 0.5 % strain for 1 hour per day for 7 days. At day 3 and day 7, the models were removed from culture and cut into quarters in both the sagittal plane and the transverse plane. These quarters were then processed for biochemical, histological, immunofluorescence, micro-computed tomography and PCR analyses. Static control groups were also included for all experimental conditions.

5.6 Biochemical Analyses

5.6.1 DNA Assay

DNA content was measured at each time point. Models were washed twice with phosphate buffered saline (PBS), weighed and then stored at -80°C. Models were then thawed and digested with 3.88 U/mL papain in

0.1 M sodium acetate, 5 mM L-cysteine-HCl, 0.05 M EDTA, pH 6.0 at 60°C under constant rotation for 18 h. DNA content was evaluated using the Hoechst 33258 DNA assay as previously described [70].

5.6.2 Extracellular ALP activity

Culture medium was collected for each experimental group and analyzed for ALP secreted into the media. At each time point models were maintained in an incubator for 2 hours, after the last bout of mechanical stimulation, before media was removed and stored at -80°C. ALP activity was determined using a colorimetric assay of enzyme activity (SIGMAFAST p-NPP Kit), which uses p-nitrophenyl phosphate (pNPP) (nmol) as a phosphatase substrate, with ALP enzyme as a standard. After thawing, 40 µL of the medium was added to a 96-well plate in triplicate with a 50 µL of pNPP solution. The plate was shielded from direct light at room temperature for one hour. Colorimetric readings were taken at 405 nm using a microplate reader (Synergy HT Multi-mode), and converted to ALP activity by creating a standard ALP curve. ALP production was also normalised to DNA content to establish whether changes in mineralization were related to the overall mineral capacity of individual cells.

5.6.3 Mineralization

Calcium content within models was determined using a Calcium Liquicolour kit (Stanbio Laboratories, Syntec, Ireland) according to the manufacturer's protocol. At each time point, models were washed twice with PBS, weighed and stored at -80°C. Models were then thawed and digested by adding 1 mL of 1M hydrochloric acid (HCl) to each model and maintained at 60°C under constant rotation for 18 h. For each of the digested models and assay standards 10 µL was added to a 96-well plate and 200 µL of the working solution was added. The plate was read using a microplate reader at an absorbance of 550 nm, as previously described[71].

5.7 Histology

At each time point samples from each group were fixed in 4% paraformaldehyde (PFA) overnight, equilibrated in 30% sucrose solution, embedded in OCT embedding medium (VWR), sectioned at 20µm using a Cryostat (CM1850, Leica) and affixed to microscope slides (Fisher Scientific). The sections were stored at -20°C. Sections were then allowed to thaw and rinsed with PBS. Sections were stained with Haematoxylin and Eosin (H&E) and TRAP (all Sigma Aldrich). For H&E, sections were immersed in Mayer's Hematoxylin, before being immersed in running tap water. Slides were immersed three times in HCl/ethanol solution (1% HCl in 70% ethanol) before being stained with Eosin (Thermo scientific) for 3 minutes. Slides were then washed again with several deionised water rinses. Of note, only cells with 3 nuclei or more were considered to be osteoclasts. For TRAP, sections were rinsed with deionised water and stained for TRAP activity using a commercial kit and counterstained with Mayer's Hematoxylin for 10 seconds before being immersed in running tap water. All sections were allowed to completely air dry before mounting with DPX. Images were acquired using a light microscope (BX 43 Olympus Microscope, software cellSens).

5.8 Immunofluorescent Staining

Samples from each experimental group were stained for Actin, DAPI, cathepsin K (CTSK), Interleukin-6 (IL-6) and AVβ3. At 3 and 7 days of culture samples were fixed using 4% paraformaldehyde at 4°C overnight. Cells within the samples were permeabilized with 0.5% Triton-X in PBS for 10 min at 4°C under agitation. For staining the actin cytoskeleton and nucleus, the samples were stained with phalloidin-FITC at 1.25 µg/mL (1:400) and DAPI dilactate (1:2000), respectively.

For CTSK staining, the samples were immersed in 1% BSA blocking solution for 1h under agitation. Then these samples were incubated in Alexa Fluor 488 conjugated mouse monoclonal anti-CTSK antibody (1:100) at 4°C overnight (Merck) and then for 1h under agitation at room temperature. Samples were further counterstained with DAPI dilactate (1:2000) to stain the nucleus. For IL6, samples were incubated in goat polyclonal IL-6 antibody (Santa Cruz) (1:100) at 4°C overnight. After three washing steps in 1% BSA, the samples were incubated with Donkey anti goat Alexa 647 (Jackson ImmunoResearch) for 1 hour under agitation at room temperature. Integrin αvβ3 staining was carried out using an anti-αvβ3 antibody directly conjugated to Alexa Fluor® 488 (1:100) (Santa Cruz). Samples were further counterstained with DAPI dilactate (1:2000) and rinsed again with 1% BSA solution.

To quantify all immunofluorescent staining, Z-stack imaging was carried out using a Fluoview FV1000 confocal laser scanning microscope system (Olympus) at a magnification of 20x (oil) with a step size of 5 µm.

All stacks were obtained at the same intensity setting between groups. NIH ImageJ software was used to analyze overall fluorescence intensity from combined stacks of images at maximum intensity projections. All fluorescent intensities were measured using the integrated density of each cell with their corresponding background integrated density subtracted.

5.9 Micro-Computed Tomography (μCT)

Samples from each experimental group were fixed using 4% paraformaldehyde at 4°C overnight for micro-computed tomography (μCT). Samples from each static and mechanically stimulated group were analyzed for mineralization by μCT scanning (Scanco Medical μCT100) using the following profile: 9 mm holder, 45 kVp tube voltage, 200 μA intensity, Al filter, 5 μm voxel size, 300 ms integration time, and a frame averaging value of 2. Samples were scanned in air and paper strips were used to minimize movement within the chamber. A density threshold of 370 mg HA/cm3 (3964 Hounsfield units) was applied to exclude hydrogel material and include mineralized regions, according to previously published work [56]. A volume of interest (VOI) of 3.95 mm^3 was segmented using Scanco Medical software (Switzerland) and evaluated for mineralization properties such as bone-like mineral volume fraction (BV/TV), bone mineral density distribution (BMDD) including mineral quantity which lies below the 25th percentile (M_{low}) or above the 75th percentile (M_{high}), and full width at half max (FWHM) to assess the quantity and distribution of mineralized material within the samples.

5.10 Quantitative Real-Time PCR

Total RNA was isolated using a custom CTAB method [72]. Briefly, each sample was digested with 250 μL of RNAse-free proteinase K solution 5 mg/mL, containing 5 mM $CaCl_2$. The digested samples were mixed with 500 μL of Cetyl trimethylammonium bromide (CTAB) solution (2% [w/v], 1.4 M NaCl, 20 mM EDTA, and 100 mM Tris, pH 8) containing 1% (v/v) β-mercaptoethanol. Then 500 μL of chloroform was added to each sample and centrifuged at 14,000 g for 2 min at room temperature. The upper/aqueous phase was transferred to a fresh tube and 800 μL of isopropanol (Fisher) was added to precipitate total RNA by centrifugation (14,000 g, 15 min, room temperature). The pellet was washed with 600 μL ethanol (70% v/v) and dissolved in 20 μL RNAse-free water for 15 min at 65°C. RNA purity and yield were assessed using a spectrophotometer (DS-11 FX, DeNovix), with 260/280 and 260/230 ratios over 1.8 for all samples. 300 ng of RNA from each sample was transcribed into cDNA using Qiagen Quantinova reverse transcription kits and thermal cycler (5PRIMEG/O2, Prime). Relative gene expression was studied by quantitative real-time polymerase chain reaction (qRT-PCR). The genes of interest included osteoblast and osteocyte specific genes: bone sialoprotein (BSP) and osteopontin (OPN), dentin matrix acidic phosphoprotein 1 (DMP1) and sclerostin (SOST), osteoclast specific genes: nuclear factor of activated T cell 1 (NFATC1) and osteoclast associated receptor (OSCAR), genes associated with bone resorption: Receptor Activator for Nuclear Factor κ B Ligand (RANKL) and osteoprotegerin (OPG), and genes implicated in metastasis: Parathyroid hormone-related protein (PTHrP), Interleukin 6 (IL-6), Transforming growth factor β (TGF-β) and Tumor necrosis factor alpha (TNF-α). Rplp0 and Rpl13A were used as reference genes (Table 1). qRT-PCR was carried out with 12.5 ng of cDNA per model, using a Qiagen Quantinova SYBR Green PCR kit and a Quant Studio 5 PCR machine (Applied Biosciences). The PCR was conducted with an enzyme activation step at 95°C for 2 min, and then for 40 cycles with the following steps: 5 s denaturation at 95°C and specific annealing temperatures for each primer pair (Table 1) for 18 s. Analysis of the results was done using the Pfaffl method (Pfaffl, 2001), and the results are expressed as relative quantitative changes to samples from day 0.

Table 1. List of primers employed for qRT-PCR, including sequences (5'-3') and annealing temperatures (Tm).

Gene	Forward Primer	Reverse Primer	Tm (°C)
BSP	**CGGCGATAGTTCCGAAGAGG**	**TTTCTGCATCTCCAGCCTTCT**	**56.3**
TNF-α	**CCC TCA CAC TCA GAT CAT CTT CT**	**GCT ACG ACG TGG GCT ACA G**	**52**
TGFβ-1	**ATC TAC TGC CTC TGC CCT GA**	**ACA CAT ACG AGG CGG AAA TC**	**52**
IL-6	**GAC AAC TTT GGC ATT GTG G**	**ATG CAG GGA TGA TGT TCT G**	**54.5**
OPN	**AGCAAGAAACTCTTCCAAGCAA**	**GTGAGATTCGTCAGATTCATCCG**	**55.2**
DMP1	**AAGCTAGCCCAGAGGGACAGGCAA**	**TTATCGGCGCCGGTCCCCGTAC**	**58**

SOST	**CTTCAGGAATGATGCCACAGAGGT**	**ATCTTTGGCGTCATAGGGATGGTG**	**58**
RANKL	**CCCATCGGGTTCCCATAAAG**	**AGCAAATGTTGGCGTACAGG**	**58**
OPG	**GCCACGCAAAAGTGTGGAAT**	**TTTGGTCCCAGGCAAACTGT**	**57.5**
NFATc1	**AGGGTCGAGGTGACACTAGG**	**GAGCGGAGAAACTTTGCGG**	**58**
OSCAR	**CGTTGATCCCAGGAGTCACAA**	**GTCCTGTCGCTGATACTCCA**	**57**
PTHrP	**AACCTGCTCCCAACACCAAA**	**AATGCGTCCTTAAGCTGGGC**	**58**
RPLp0	**AGATTCGGGATATGCTGTTGGC**	**TCGGGTCCTAGACCAGTGTTC**	**58.2**
Rpl13A	**TACCAGAAAGTTTGCTTACCTGGG**	**TGCCTGTTTCCGTAACCTCAAG**	**57.3**

5.11 Statistical Analysis

Statistical analyses were performed using GraphPad Prism (version 8) software. Two-way ANOVA was used for analysis of variance with Bonferroni's post-hoc tests to compare between groups. The results are displayed as mean ± standard deviation, with significance at a level of $p \leq 0.05$. Three to four replicates were analyzed for each experimental group. The experiments were repeated 3 times.

Acknowledgments: This research was funded by IRC Laureate Award Programme 2017/18, MEMETic, IR-CLA/2017/217. The authors acknowledge the facilities and scientific and technical assistance of the Centre for Microscopy and Imaging at the National University of Ireland Galway (www.imaging.nuigalway.ie). The authors would also like to acknowledge Servier Medical Art (www.servier.com) for their image bank used to produce the figures.

Author Contributions: Conceptualization, S.M.N., V.K., E.M., L.McN.; methodology, S.M.N., V.K., A.S.K.V., E.M., L.McN.; validation S.M.N. and V.K.; formal analysis, S.M.N., V.K. and A.S.K.V.; investigation, S.M.N. and V.K.; data curation, S.M.N. and V.K.; writing—original draft preparation, S.M.N.; writing—review and editing, S.M.N., V.K., A.S.K.V., E.M., L.McN; visualization, S.M.N., V.K.; supervision, E.M., L.McN; project administration, S.M.N. and L.McN.; funding acquisition, L.McN. All authors have read and agreed to the published version of the manuscript.

Competing Interests: The authors declare no conflict of interest. The funders had no role in the design of the study; in the collection, analyses, or interpretation of data; in the writing of the manuscript, or in the decision to publish the results.

6. References

1 Mundy, G. R. Metastasis to bone: causes, consequences and therapeutic opportunities. *Nature Reviews Cancer* **2**, 584-593, doi:10.1038/nrc867 (2002).

2 Sloan, E. K. & Anderson, R. L. Genes involved in breast cancer metastasis to bone. *Cellular and Molecular Life Sciences CMLS* **59**, 1491-1502, doi:10.1007/s00018-002-8524-5 (2002).

3 Thomas, R. C. *et al.* Bone: A Fertile Soil for Cancer Metastasis. *Current Drug Targets* **18**, 1281-1295, doi:http://dx.doi.org/10.2174/1389450117666161226121650 (2017).

4 Waning, D. L. & Guise, T. A. Molecular mechanisms of bone metastasis and associated muscle weakness. *Clin Cancer Res* **20**, 3071-3077, doi:10.1158/1078-0432.CCR-13-1590 (2014).

5 Guise, T. A. Molecular mechanisms of osteolytic bone metastases. *Cancer* **88**, 2892-2898, doi:10.1002/1097-0142(20000615)88:12+<2892::Aid-cncr2>3.0.Co;2-y (2000).

6 Jin, X. & Mu, P. Targeting Breast Cancer Metastasis. *Breast Cancer (Auckl)* **9**, 23-34, doi:10.4137/BCBCR.S25460 (2015).

7 Paszek, M. J. & Weaver, V. M. The Tension Mounts: Mechanics Meets Morphogenesis and Malignancy. *Journal of Mammary Gland Biology and Neoplasia* **9**, 325-342, doi:10.1007/s10911-004-1404-x (2004).

8 Albelda, S. *et al.* Integrin Distribution in Malignant Melanoma: Association of the ??3 Subunit with Tumor Progression. *Cancer research* **50**, 6757-6764 (1990).

9 Pignatelli, M., Cardillo, M. R., Hanby, A. & Stamp, G. W. H. Integrins and their accessory adhesion molecules in mammary carcinomas: Loss of polarization in poorly differentiated tumors. *Human Pathology* **23**, 1159-1166, doi:https://doi.org/10.1016/0046-8177(92)90034-Z (1992).

10 Zaman, M. H. *et al.* Migration of tumor cells in 3D matrices is governed by matrix stiffness along with cell-matrix adhesion and proteolysis. *Proceedings of the National Academy of Sciences of the United States of America* **103**, 10889-10894, doi:10.1073/pnas.0604460103 (2006).

11 Suresh, S. Biomechanics and biophysics of cancer cells. *Acta biomaterialia* **3**, 413-438, doi:10.1016/j.actbio.2007.04.002 (2007).

12 Makale, M. Cellular mechanobiology and cancer metastasis. *Birth Defects Research Part C: Embryo Today: Reviews* **81**, 329-343, doi:10.1002/bdrc.20110 (2007).

13 Guo, W. & Giancotti, F. G. Integrin signalling during tumour progression. *Nature Reviews Molecular Cell Biology* **5**, 816-826, doi:10.1038/nrm1490 (2004).

14 Ingber, D. Mechanobiology and diseases of mechanotransduction. *Annals of Medicine* **35**, 564-577, doi:10.1080/07853890310016333 (2003).

15 Walker, C., Mojares, E. & Del Río Hernández, A. Role of Extracellular Matrix in Development and Cancer Progression. *International journal of molecular sciences* **19**, doi:10.3390/ijms19103028 (2018).

16 Fenner, J. *et al.* Macroscopic Stiffness of Breast Tumors Predicts Metastasis. *Scientific Reports* **4**, 5512, doi:10.1038/srep05512 (2014).

17 Plewes, D. B., Bishop, J., Samani, A. & Sciarretta, J. Visualization and quantification of breast cancer biomechanical properties with magnetic resonance elastography. *Physics in Medicine and Biology* **45**, 1591-1610, doi:10.1088/0031-9155/45/6/314 (2000).

18 Krouskop, T. A., Wheeler, T. M., Kallel, F., Garra, B. S. & Hall, T. Elastic Moduli of Breast and Prostate Tissues under Compression. *Ultrasonic Imaging* **20**, 260-274, doi:10.1177/016173469802000403 (1998).

19 Ulrich, T. A., de Juan Pardo, E. M. & Kumar, S. The mechanical rigidity of the extracellular matrix regulates the structure, motility, and proliferation of glioma cells. *Cancer research* **69**, 4167-4174, doi:10.1158/0008-5472.CAN-08-4859 (2009).

20 Paszek, M. J. *et al.* Tensional homeostasis and the malignant phenotype. *Cancer Cell* **8**, 241-254, doi:10.1016/j.ccr.2005.08.010 (2005).

21 Kostic, A., Lynch, C. D. & Sheetz, M. P. Differential matrix rigidity response in breast cancer cell lines correlates with the tissue tropism. *PLoS One* **4**, e6361, doi:10.1371/journal.pone.0006361 (2009).

22 Page, J. M. *et al.* Matrix rigidity regulates the transition of tumor cells to a bone-destructive phenotype through integrin beta3 and TGF-beta receptor type II. *Biomaterials* **64**, 33-44, doi:10.1016/j.biomaterials.2015.06.026 (2015).

23 Nazarian, A., von Stechow, D., Zurakowski, D., Müller, R. & Snyder, B. D. Bone Volume Fraction Explains the Variation in Strength and Stiffness of Cancellous Bone Affected by Metastatic Cancer and Osteoporosis. *Calcified Tissue International* **83**, 368-379, doi:10.1007/s00223-008-9174-x (2008).

24 Kaneko, T. S., Bell, J. S., Pejcic, M. R., Tehranzadeh, J. & Keyak, J. H. Mechanical properties, density and quantitative CT scan data of trabecular bone with and without metastases. *Journal of Biomechanics* **37**, 523-530, doi:https://doi.org/10.1016/j.jbiomech.2003.08.010 (2004).

25 Canon, J. R. *et al.* Inhibition of RANKL blocks skeletal tumor progression and improves survival in a mouse model of breast cancer bone metastasis. *Clin Exp Metastasis* **25**, 119-129, doi:10.1007/s10585-007-9127-1 (2008).

26 Thibaudeau, L. *et al.* A tissue-engineered humanized xenograft model of human breast cancer metastasis to bone. *Dis Model Mech* **7**, 299-309, doi:10.1242/dmm.014076 (2014).

596 27 Yoneda, T., Williams, P. J., Hiraga, T., Niewolna, M. & Nishimura, R. A bone-seeking clone exhibits different biological
597 properties from the MDA-MB-231 parental human breast cancer cells and a brain-seeking clone in vivo and in vitro. *J Bone*
598 *Miner Res* **16**, 1486-1495, doi:10.1359/jbmr.2001.16.8.1486 (2001).
599 28 Khalili, P., Arakelian, A., Chen, G., Singh, G. & Rabbani, S. A. Effect of Herceptin on the development and progression of
600 skeletal metastases in a xenograft model of human breast cancer. *Oncogene* **24**, 6657-6666, doi:10.1038/sj.onc.1208790 (2005).
601 29 Harms, J. F. *et al.* A small molecule antagonist of the alpha(v)beta3 integrin suppresses MDA-MB-435 skeletal metastasis.
602 *Clin Exp Metastasis* **21**, 119-128 (2004).
603 30 Acha, A., Ruesga, M. T., Rodriguez, M. J., Martinez de Pancorbo, M. A. & Aguirre, J. M. Applications of the oral scraped
604 (exfoliative) cytology in oral cancer and precancer. *Med Oral Patol Oral Cir Bucal* **10**, 95-102, doi:10488991 [pii] (2005).
605 31 Baker, B. M. & Chen, C. S. Deconstructing the third dimension: how 3D culture microenvironments alter cellular cues. *J Cell*
606 *Sci* **125**, 3015-3024, doi:10.1242/jcs.079509 (2012).
607 32 Salamanna, F. *et al.* An in vitro 3D bone metastasis model by using a human bone tissue culture and human sex-related
608 cancer cells. *Oncotarget* **7**, 76966-76983, doi:10.18632/oncotarget.12763 (2016).
609 33 Salamanna, F. *et al.* A Human 3D In Vitro Model to Assess the Relationship Between Osteoporosis and Dissemination to
610 Bone of Breast Cancer Tumor Cells. *J Cell Physiol* **232**, 1826-1834, doi:10.1002/jcp.25708 (2017).
611 34 Bock, N. *et al.* In vitro engineering of a bone metastases model allows for study of the effects of antiandrogen therapies in
612 advanced prostate cancer. *Sci Adv* **7**, eabg2564, doi:10.1126/sciadv.abg2564 (2021).
613 35 Colombo, M. V. *et al.* Engineering the early bone metastatic niche through human vascularized immuno bone minitissues.
614 *Biofabrication* **13**, doi:10.1088/1758-5090/abefea (2021).
615 36 Han, W. *et al.* In vitro bone metastasis dwelling in a 3D bioengineered niche. *Biomaterials* **269**, 120624,
616 doi:https://doi.org/10.1016/j.biomaterials.2020.120624 (2021).
617 37 Choi, S. *et al.* Biofunctional matrix models reveal mineral-dependent mechanoregulation of bone metastatic breast cancer.
618 *bioRxiv*, 2022.2006.2029.498001, doi:10.1101/2022.06.29.498001 (2022).
619 38 Curtis, K. J. *et al.* Mechanical stimuli and matrix properties modulate cancer spheroid growth in three-dimensional gelatin
620 culture. *Journal of The Royal Society Interface* **17**, 20200568, doi:doi:10.1098/rsif.2020.0568 (2020).
621 39 Lynch, M. E. *et al.* In vivo tibial compression decreases osteolysis and tumor formation in a human metastatic breast cancer
622 model. *J Bone Miner Res* **28**, 2357-2367, doi:10.1002/jbmr.1966 (2013).
623 40 Fan, Y. *et al.* Skeletal loading regulates breast cancer-associated osteolysis in a loading intensity-dependent fashion. *Bone Res*
624 **8**, 9, doi:10.1038/s41413-020-0083-6 (2020).
625 41 Jansen, L. E., Birch, N. P., Schiffman, J. D., Crosby, A. J. & Peyton, S. R. Mechanics of intact bone marrow. *J Mech Behav*
626 *Biomed Mater* **50**, 299-307, doi:10.1016/j.jmbbm.2015.06.023 (2015).
627 42 Rodriguez, E. K., Hoger, A. & McCulloch, A. D. Stress-dependent finite growth in soft elastic tissues. *J Biomech* **27**, 455-467,
628 doi:10.1016/0021-9290(94)90021-3 (1994).
629 43 Ambrosi, D., Pezzuto, S., Riccobelli, D., Stylianopoulos, T. & Ciarletta, P. Solid tumors are poroelastic solids with a chemo-
630 mechanical feedback on growth. *J Elast* **129**, 107-124, doi:10.1007/s10659-016-9619-9 (2017).
631 44 Tan, S. D. *et al.* Osteocytes subjected to fluid flow inhibit osteoclast formation and bone resorption. *Bone* **41**, 745-751,
632 doi:10.1016/j.bone.2007.07.019 (2007).
633 45 You, L. *et al.* Osteocytes as mechanosensors in the inhibition of bone resorption due to mechanical loading. *Bone* **42**, 172-179,
634 doi:10.1016/j.bone.2007.09.047 (2008).
635 46 Verbruggen, A. S. K., McCarthy, E. C., Dwyer, R. M. & McNamara, L. M. Temporal and spatial changes in bone mineral
636 content and mechanical properties during breast-cancer bone metastases. *Bone Rep* **17**, 101597,
637 doi:10.1016/j.bonr.2022.101597 (2022).

638 47 Burke, M. *et al.* The impact of metastasis on the mineral phase of vertebral bone tissue. *J Mech Behav Biomed Mater* **69**, 75-84,
639 doi:10.1016/j.jmbbm.2016.12.017 (2017).
640 48 Parle, E. *et al.* Bone Mineral Is More Heterogeneously Distributed in the Femoral Heads of Osteoporotic and Diabetic
641 Patients: A Pilot Study. *JBMR Plus* **4**, e10253, doi:10.1002/jbm4.10253 (2020).
642 49 Zhao, F., Vaughan, T. J. & McNamara, L. M. Multiscale fluid-structure interaction modelling to determine the mechanical
643 stimulation of bone cells in a tissue engineered scaffold. *Biomech Model Mechanobiol* **14**, 231-243, doi:10.1007/s10237-014-0599-
644 z (2015).
645 50 Park, P. H., McMullen, M. R., Huang, H., Thakur, V. & Nagy, L. E. Short-term treatment of RAW264.7 macrophages with
646 adiponectin increases tumor necrosis factor-alpha (TNF-alpha) expression via ERK1/2 activation and Egr-1 expression: role
647 of TNF-alpha in adiponectin-stimulated interleukin-10 production. *J Biol Chem* **282**, 21695-21703,
648 doi:10.1074/jbc.M701419200 (2007).
649 51 Ueshima, E. *et al.* Macrophage-secreted TGF-beta1 contributes to fibroblast activation and ureteral stricture after ablation
650 injury. *Am J Physiol Renal Physiol* **317**, F52-F64, doi:10.1152/ajprenal.00260.2018 (2019).
651 52 Bray, L. J. *et al.* Three-Dimensional In Vitro Hydro- and Cryogel-Based Cell-Culture Models for the Study of Breast-Cancer
652 Metastasis to Bone. *Cancers (Basel)* **10**, doi:10.3390/cancers10090292 (2018).
653 53 Wang, X. & Lin, Y. Tumor necrosis factor and cancer, buddies or foes? *Acta Pharmacol Sin* **29**, 1275-1288, doi:10.1111/j.1745-
654 7254.2008.00889.x (2008).
655 54 Burow, M. E. *et al.* Differences in susceptibility to tumor necrosis factor alpha-induced apoptosis among MCF-7 breast cancer
656 cell variants. *Cancer Res* **58**, 4940-4946 (1998).
657 55 Yoshitake, F., Itoh, S., Narita, H., Ishihara, K. & Ebisu, S. Interleukin-6 directly inhibits osteoclast differentiation by
658 suppressing receptor activator of NF-kappaB signaling pathways. *J Biol Chem* **283**, 11535-11540, doi:10.1074/jbc.M607999200
659 (2008).
660 56 Naqvi, S. M., Panadero Pérez, J. A., Kumar, V., Verbruggen, A. S. K. & McNamara, L. M. A Novel 3D Osteoblast and
661 Osteocyte Model Revealing Changes in Mineralization and Pro-osteoclastogenic Paracrine Signaling During Estrogen
662 Deficiency. *Frontiers in Bioengineering and Biotechnology* **8**, doi:10.3389/fbioe.2020.00601 (2020).
663 57 Rubin, J., Rubin, C. & Jacobs, C. R. Molecular pathways mediating mechanical signaling in bone. *Gene* **367**, 1-16,
664 doi:10.1016/j.gene.2005.10.028 (2006).
665 58 el Haj, A. J., Minter, S. L., Rawlinson, S. C., Suswillo, R. & Lanyon, L. E. Cellular responses to mechanical loading in vitro. *J*
666 *Bone Miner Res* **5**, 923-932, doi:10.1002/jbmr.5650050905 (1990).
667 59 Duty, A. O., Oest, M. E. & Guldberg, R. E. Cyclic mechanical compression increases mineralization of cell-seeded polymer
668 scaffolds in vivo. *J Biomech Eng* **129**, 531-539, doi:10.1115/1.2746375 (2007).
669 60 Baas, E., Kuiper, J. H., Yang, Y., Wood, M. A. & El Haj, A. J. In vitro bone growth responds to local mechanical strain in
670 three-dimensional polymer scaffolds. *J Biomech* **43**, 733-739, doi:10.1016/j.jbiomech.2009.10.016 (2010).
671 61 Ravichandran, A. *et al.* In vitro cyclic compressive loads potentiate early osteogenic events in engineered bone tissue. *J*
672 *Biomed Mater Res B Appl Biomater* **105**, 2366-2375, doi:10.1002/jbm.b.33772 (2017).
673 62 Sittichokechaiwut, A., Edwards, J. H., Scutt, A. M. & Reilly, G. C. Short bouts of mechanical loading are as effective as
674 dexamethasone at inducing matrix production by human bone marrow mesenchymal stem cell. *Eur Cell Mater* **20**, 45-57,
675 doi:vol020a05 [pii] (2010).
676 63 Sittichockechaiwut, A., Scutt, A. M., Ryan, A. J., Bonewald, L. F. & Reilly, G. C. Use of rapidly mineralising osteoblasts and
677 short periods of mechanical loading to accelerate matrix maturation in 3D scaffolds. *Bone* **44**, 822-829,
678 doi:10.1016/j.bone.2008.12.027 (2009).

679 64 Negishi-Koga, T. *et al.* Suppression of bone formation by osteoclastic expression of semaphorin 4D. *Nat Med* **17**, 1473-1480,
680 doi:10.1038/nm.2489 (2011).
681 65 Soki, F. N., Park, S. I. & McCauley, L. K. The multifaceted actions of PTHrP in skeletal metastasis. *Future Oncol* **8**, 803-817,
682 doi:10.2217/fon.12.76 (2012).
683 66 Wu, Q., Zhou, X., Huang, D., Ji, Y. & Kang, F. IL-6 Enhances Osteocyte-Mediated Osteoclastogenesis by Promoting JAK2
684 and RANKL Activity In Vitro. *Cell Physiol Biochem* **41**, 1360-1369, doi:10.1159/000465455 (2017).
685 67 Yoneda, T. *et al.* Actions of bisphosphonate on bone metastasis in animal models of breast carcinoma. *Cancer* **88**, 2979-2988,
686 doi:https://doi.org/10.1002/1097-0142(20000615)88:12+<2979::AID-CNCR13>3.0.CO;2-U (2000).
687 68 Bacabac, R. G. *et al.* Nitric oxide production by bone cells is fluid shear stress rate dependent. *Biochem Biophys Res Commun*
688 **315**, 823-829, doi:10.1016/j.bbrc.2004.01.138 (2004).
689 69 Mullender, M. G. *et al.* Release of nitric oxide, but not prostaglandin E2, by bone cells depends on fluid flow frequency. *J*
690 *Orthop Res* **24**, 1170-1177, doi:10.1002/jor.20179 (2006).
691 70 Haugh, M. G. *et al.* Temporal and spatial changes in cartilage-matrix-specific gene expression in mesenchymal stem cells in
692 response to dynamic compression. *Tissue Eng Part A* **17**, 3085-3093, doi:10.1089/ten.tea.2011.0198 (2011).
693 71 Freeman, F. E., Haugh, M. G. & McNamara, L. M. An in vitro bone tissue regeneration strategy combining chondrogenic
694 and vascular priming enhances the mineralization potential of mesenchymal stem cells in vitro while also allowing for
695 vessel formation. *Tissue Eng Part A* **21**, 1320-1332, doi:10.1089/ten.TEA.2014.0249 (2015).
696 72 Köster, N. *et al.* Single-Step RNA Extraction from Different Hydrogel-Embedded Mesenchymal Stem Cells for Quantitative
697 Reverse Transcription-Polymerase Chain Reaction Analysis. *Tissue Eng Part C Methods* **22**, 552-560,
698 doi:10.1089/ten.TEC.2015.0362 (2016).
699
700

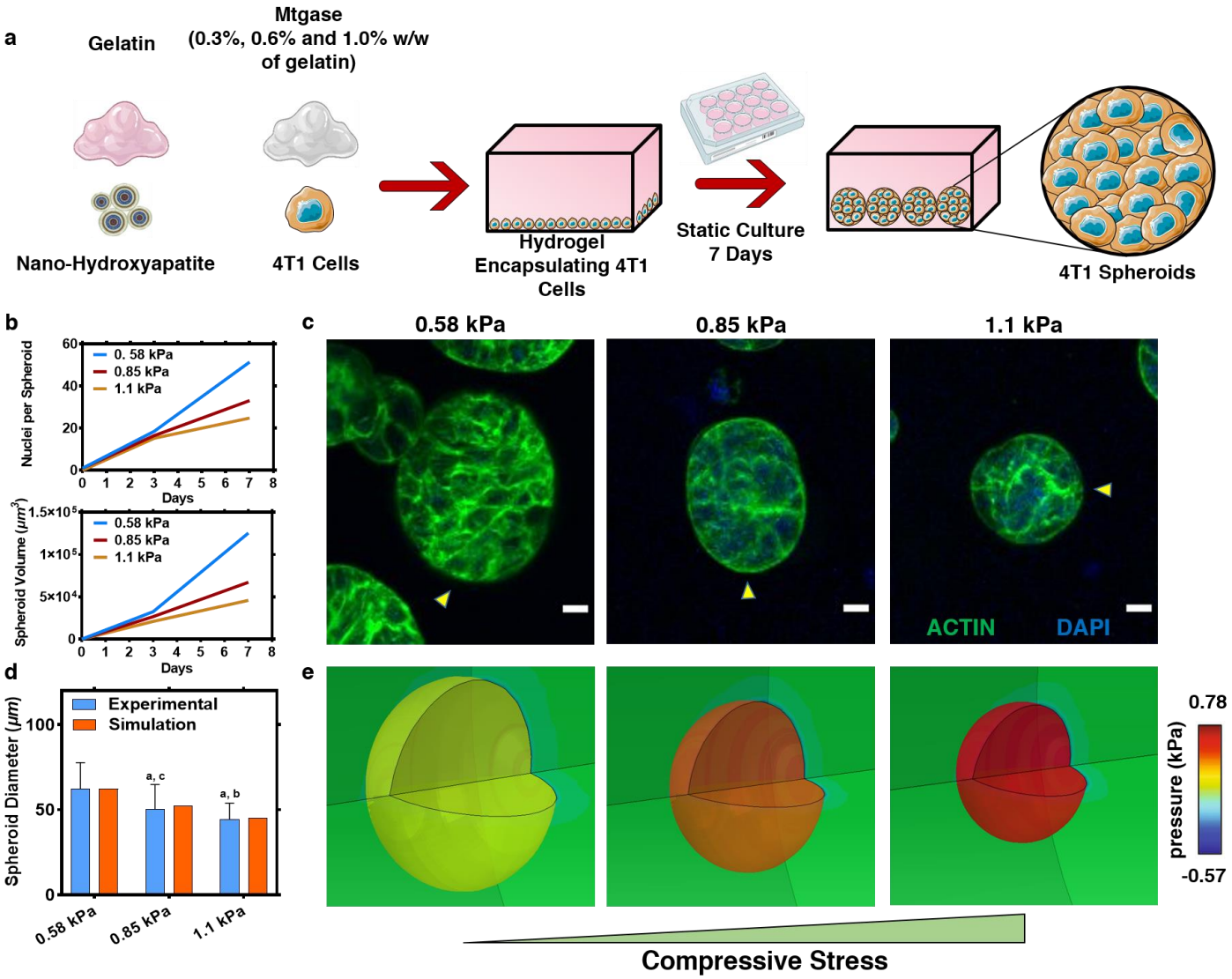

Figure 1: 4T1 mammary carcinoma cells encapsulated in gelatin hydrogels of different compression modulus (0.58 kPa, 0.85 kPa and 1.1 kPa) form spheroids whose growth is sensitive to stress imposed by the hydrogels. a, Schematic of the process of encapsulation 4T1 cells in single suspension within gelatin-transglutaminase hydrogels and static culture and growth of tumor cells into spheroids. b, Nuclei per 4T1 tumor spheroid and spheroid volume over time across three compression modulus. c, fluorescently stained 4T1 spheroids (arrow) within the hydrogels for Actin (green) and Dapi (blue) at day 7 (scale bar: 10 μm). d, Comparison of tumor spheroids in the hydrogels at day 7 of culture with results of simulation from computational tumor growth model within the hydrogels of 0.58 kPa, 0.85 kPa and 1.1 kPa compression modulus. e, Computational model simulation of spheroid growth within the hydrogels (represented by the green background) the resulting stresses that develop. #, a, b, c: significance compared to 4T1 monoculture, 0.58 kPa, 0.85 kPa and 1.1 kPa, respectively.

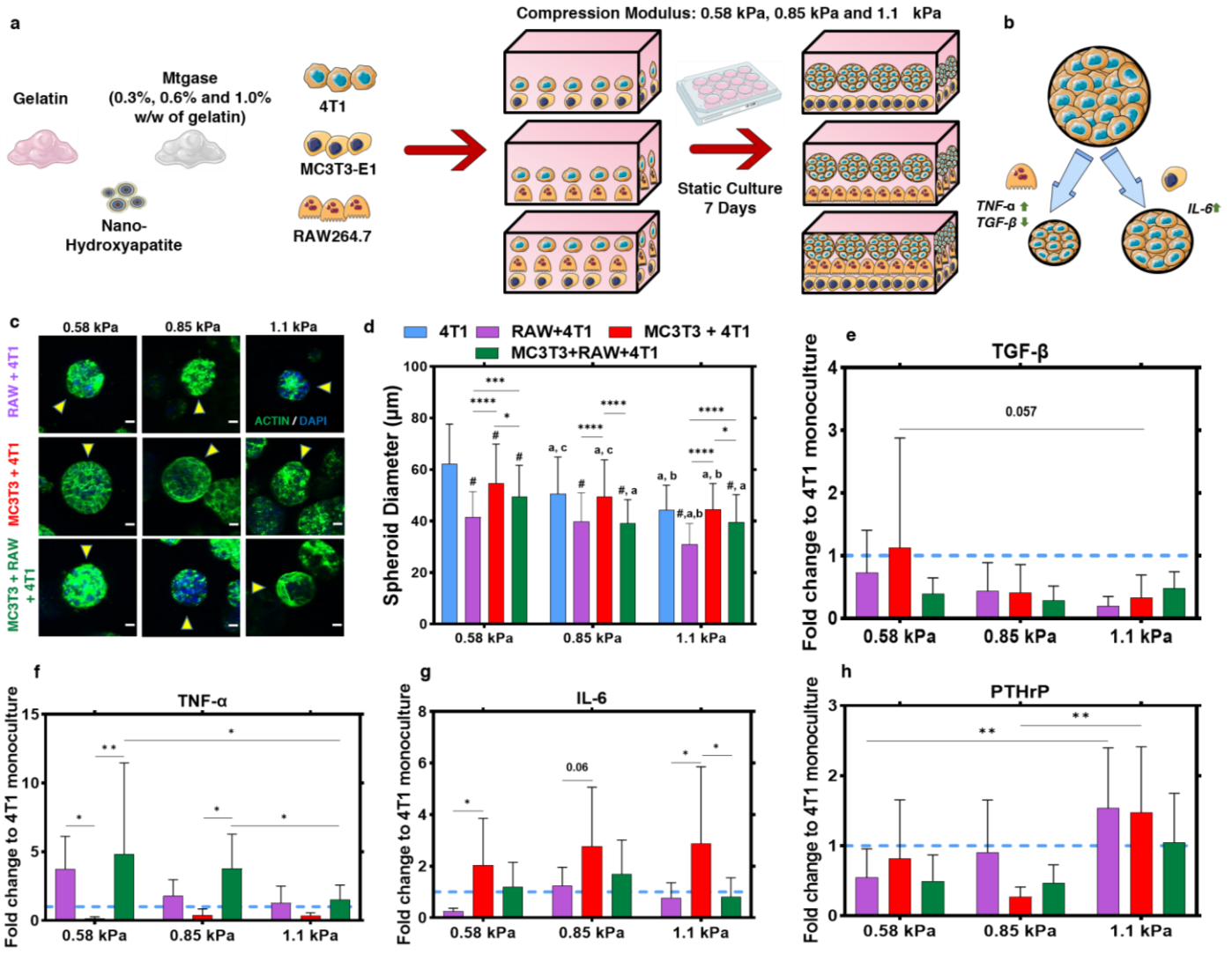

Figure 2: Inclusion of bone cells in culture with 4T1 cells in a co-culture and tri-culture configuration: Osteoclasts have an inhibitory effect on 4T1 spheroid growth which is partially mitigated by osteoblasts. a, Schematic of the process of encapsulation RAW264.7 (Osteoclast Precursors) and MC3T3-E1 (Osteoblast) with 4T1 cells in co-culture and tri-culture configurations within gelatin-transglutaminase hydrogels and static culture and growth of tumor cells into spheroids. **b,** Schematic depicting the effect of individual bone cells on the tumor spheroid. **c**, fluorescently stained 4T1 spheroids (yellow arrows) within the hydrogels for Actin (green) and Dapi (blue) at day 7 (scale bar: 10 µm) in the co-culture and tri-culture configuration with bone cells. **d**, Quantification of the 4T1 spheroid size. **e-h**, qRT-PCR analysis for, TGF-β, TNF-α, IL-6 and PTHrP. #, a, b, c: significance compared to 4T1 monoculture, 0.58 kPa, 0.85 kPa and 1.1 kPa, respectively *: P <0.05, **:P<0.01, ***:P<0.001, ****:P<0.0001.

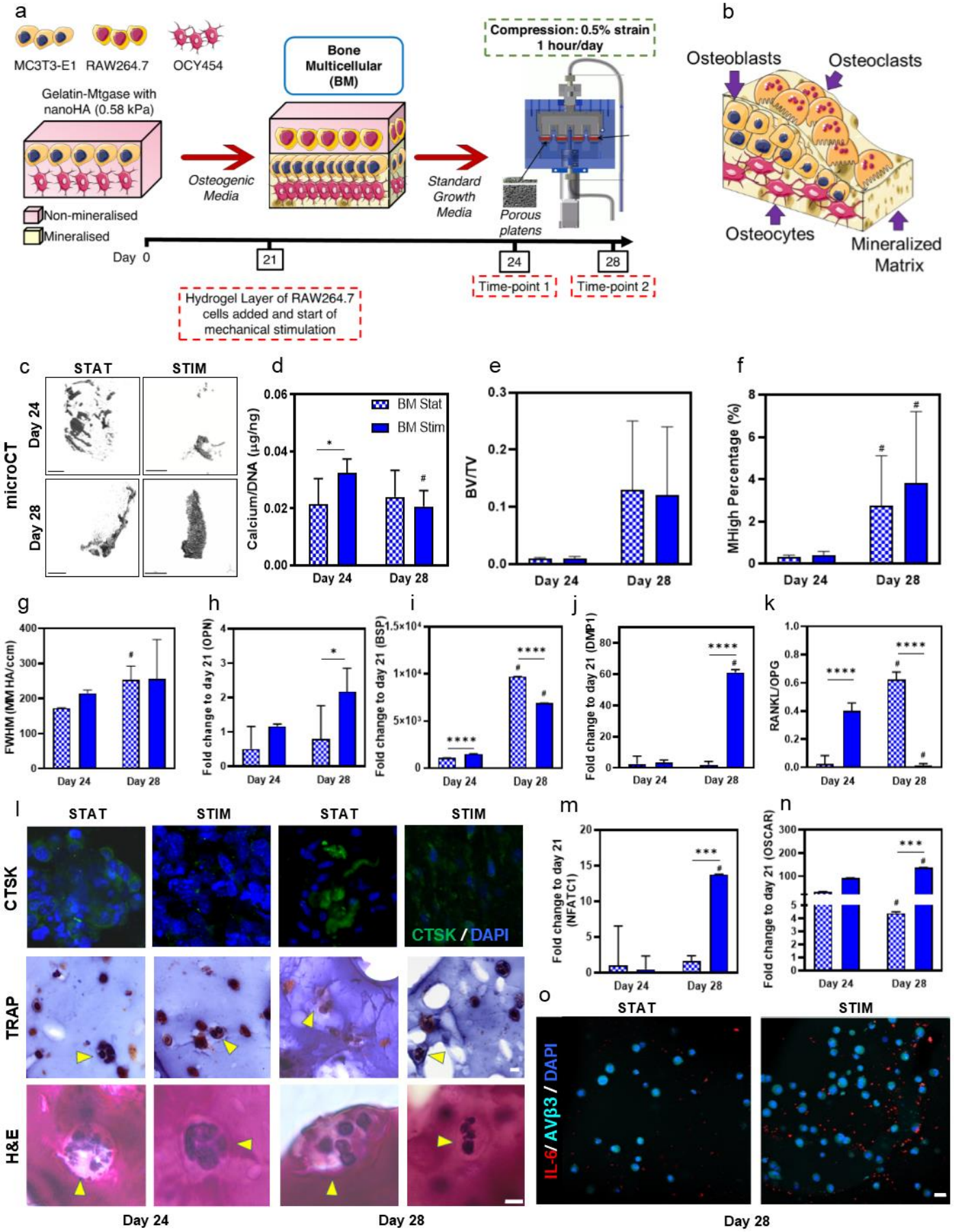
a
MC3T3-E1
RAW264.7
OCY454
Gelatin-Mtgase with nanoHA (0.58 kPa)
Non-mineralised
Mineralised
Osteogenic Media
Bone Multicellular (BM)
Standard Growth Media
Compression: 0.5% strain 1 hour/day
Porous platens
Day 0
21
24
28
Time-point 1
Time-point 2
Hydrogel Layer of RAW264.7 cells added and start of mechanical stimulation
b
Osteoblasts
Osteoclasts
Osteocytes
Mineralized Matrix
c
STAT
STIM
microCT
Day 24
Day 28
d
Calcium/DNA (µg/ng)
BM Stat
BM Stim
Day 24
Day 28
e
BV/TV
Day 24
Day 28
f
MHigh Percentage (%)
Day 24
Day 28
g
FWHM (MM HA/ccm)
Day 24
Day 28
h
Fold change to day 21 (OPN)
Day 24
Day 28
i
Fold change to day 21 (BSP)
Day 24
Day 28
j
Fold change to day 21 (DMP1)
Day 24
Day 28
k
RANKL/OPG
Day 24
Day 28
l
STAT
STIM
STAT
STIM
CTSK
TRAP
H&E
CTSK / DAPI
Day 24
Day 28
m
Fold change to day 21 (NFATC1)
Day 24
Day 28
n
Fold change to day 21 (OSCAR)
Day 24
Day 28
o
STAT
STIM
IL-6/ AVβ3 / DAPI
Day 28

725

Figure 3: Bone Multicellular (BM) model have mineral deposits, osteoblastic activity and the presence of active osteoclasts in them. a, Schematic of the timeline and the process of encapsulation of OCY 454 and MC3T3-E1 cells within gelatin-transglutaminase hydrogels followed by culture in osteogenic media for 3 weeks followed by the addition of a layer of hydrogel encapsulating RAW264.7 cells and the application of mechanical compression for 7 days. **b**, Schematic depicting the *in vitro* mineralized bone-multicellular model with active osteoclasts. **c**, Micro-CT analysis of the models (scale bar: 1 mm). **d**, Calcium content in the models. **e**, Bone-like mineral volume fraction (BV/TV). **f**, MHigh percentage. **g**, FWHM. **h**, qRT-PCR analysis for OPN expression in the BM model. **i**, qRT-PCR analysis for BSP expression. **j**, qRT-PCR analysis for DMP1 expression. **k,** RANKL/OPG. **l**, Immunofluorescence staining for CTSK and Histology for TRAP (scale bar: 20 µm) and H&E (scale bar: 10 µm) in the BM model **m**, qRT-PCR analysis for NFATC1 expression. **n**, qRT-PCR analysis for OSCAR expression. **o**, Immunofluorescence for IL-6 and Avβ3 day 28 in the BM model (scale bar: 20 µm). #: significance compared to day 24, *:P <0.05, **:P<0.01, ***:P<0.001, ****:P<0.0001.

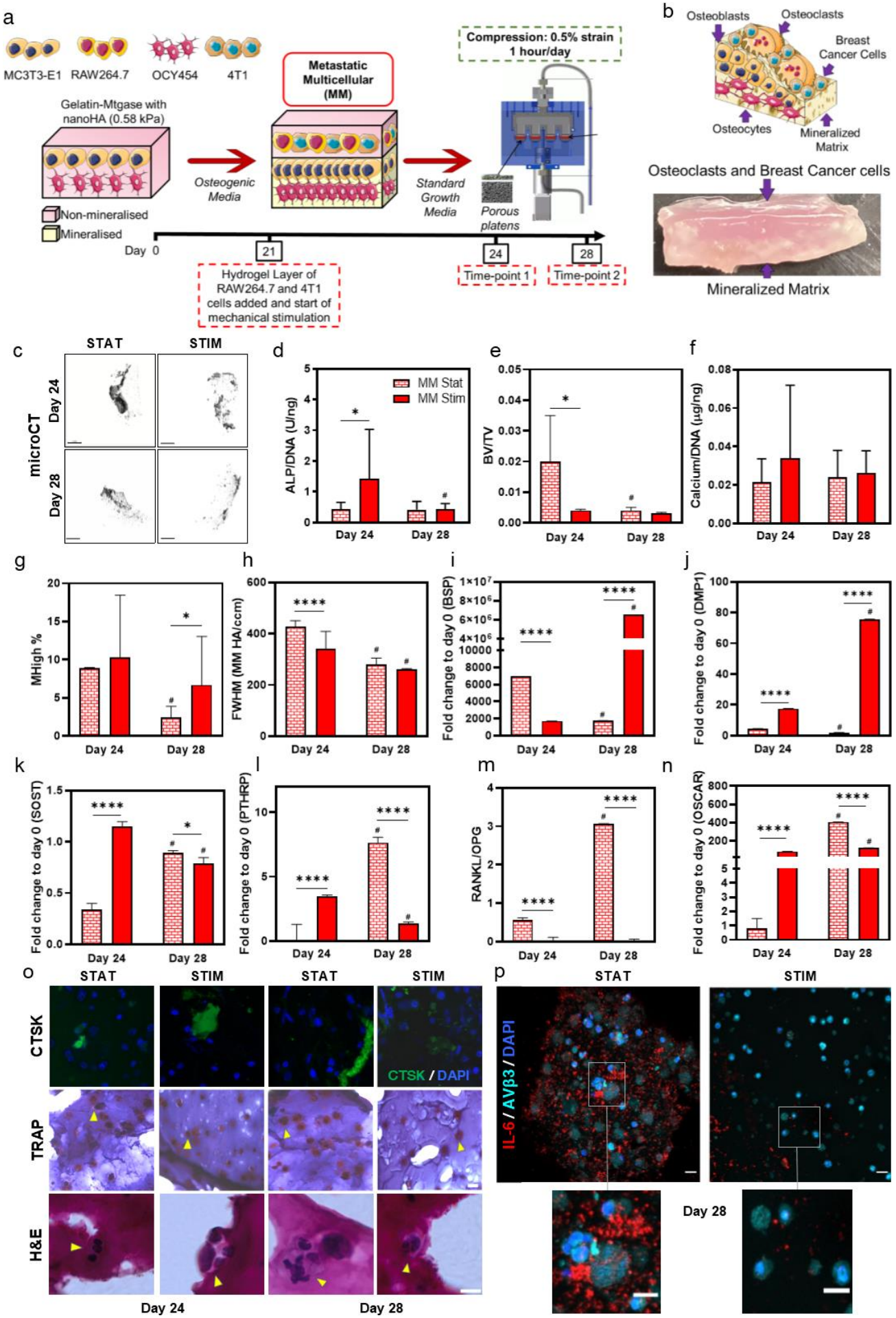
a
MC3T3-E1
RAW264.7
OCY454
4T1
Gelatin-Mtgase with nanoHA (0.58 kPa)
Non-mineralised
Mineralised
Osteogenic Media
Metastatic Multicellular (MM)
Standard Growth Media
Compression: 0.5% strain 1 hour/day
Porous platens
Day 0
21
24
28
Hydrogel Layer of RAW264.7 and 4T1 cells added and start of mechanical stimulation
Time-point 1
Time-point 2
b
Osteoblasts
Osteoclasts
Breast Cancer Cells
Osteocytes
Mineralized Matrix
Osteoclasts and Breast Cancer cells
Mineralized Matrix
c
STAT
STIM
microCT
Day 24
Day 28
d
MM Stat
MM Stim
ALP/DNA (U/ng)
e
BV/TV
f
Calcium/DNA (μg/ng)
g
MHigh %
h
FWHM (MM HA/ccm)
i
Fold change to day 0 (BSP)
j
Fold change to day 0 (DMP1)
k
Fold change to day 0 (SOST)
l
Fold change to day 0 (PTHRP)
m
RANKL/OPG
n
Fold change to day 0 (OSCAR)
o
CTSK
TRAP
H&E
CTSK / DAPI
p
IL-6 / AVβ3 / DAPI

740

Figure 4: Metastatic Multicellular model exhibit osteolytic metastatic response which is attenuated under mechanical compression. a, Schematic of the timeline and the process of encapsulation of OCY 454 and MC3T3-E1 cells within gelatin-transglutaminase hydrogels followed by culture in osteogenic media for 3 weeks followed by the addition of a layer of hydrogel encapsulating RAW264.7 and 4T1 cells and the application of mechanical compression for 7 days. **b**, Schematic depicting the *in vitro* mineralized metastatic-multicellular model with active osteoclasts and image (bottom) of the mineralized multicellular model with the bottom mineralized layer and the top layer with osteoclasts and breast cancer cells. **c**, Micro-CT analysis of the models (scale bar: 1 mm). **d**, ALP activity. **e**, Calcium content in the models. **f**, Bone-like mineral volume fraction (BV/TV). **g**, MHigh percentage. **h**, FWHM. **i**, qRT-PCR analysis for BSP expression in the MM model. **j**, qRT-PCR analysis for DMP1 expression. **k**, qRT-PCR analysis for SOST expression. **l**, qRT-PCR analysis for PTHrP expression. **m**, RANKL/OPG. **n**, qRT-PCR analysis for OSCAR expression. **o**, Immunofluorescence staining for CTSK and Histology for TRAP (scale bar: 20 µm) and H&E (scale bar: 10 µm) in the MM model. **p**, Immunofluorescence for IL-6 and AVβ3 day 28 in the MM model (scale bar: 20 µm). #: significance compared to day 24, *:P <0.05, **:P<0.01, ***:P<0.001, ****:P<0.0001.

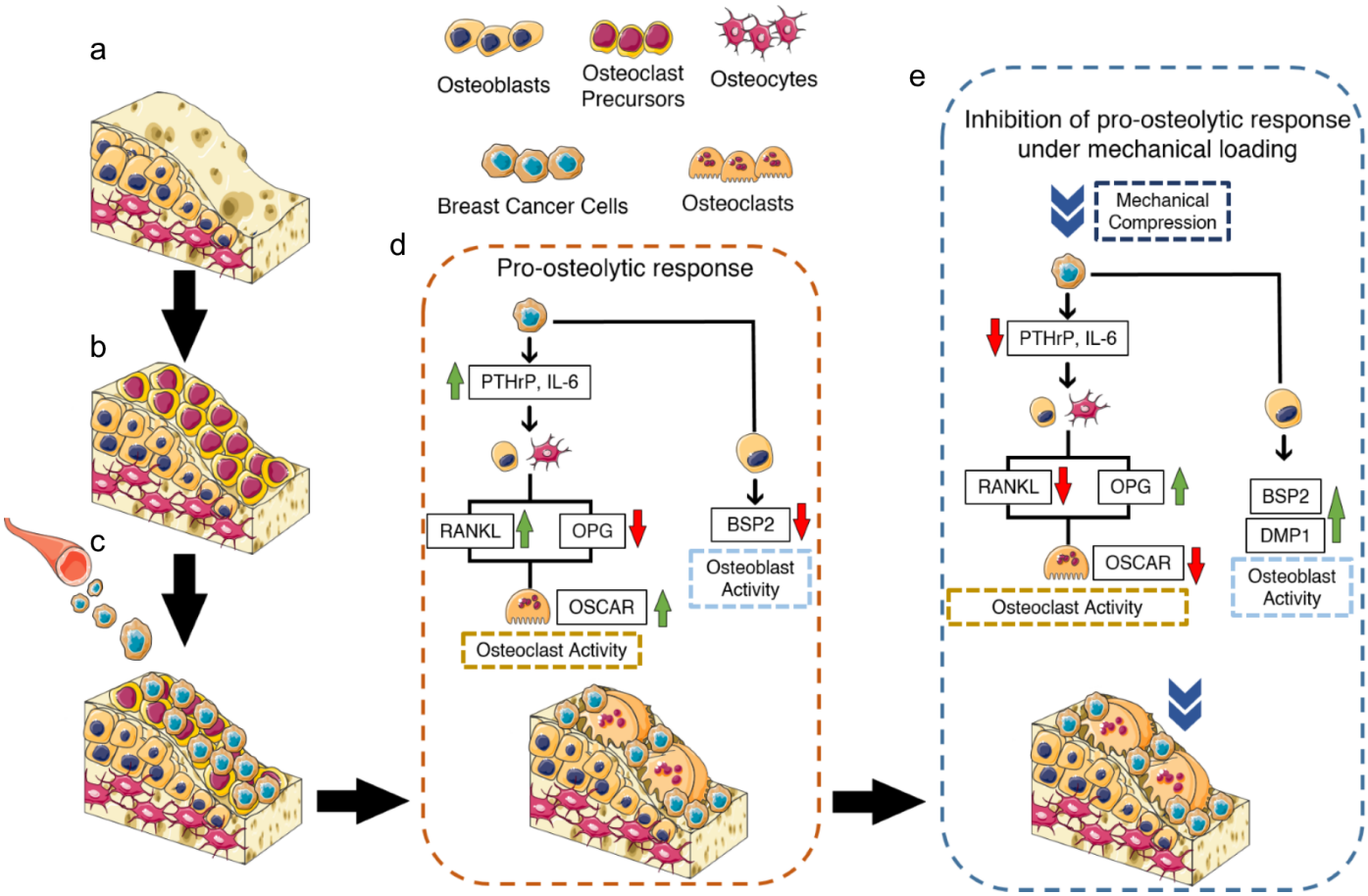

Figure 5: Mimicking the osteolytic metastatic process using the 3D *in vitro* multicellular mineralized and highlighting the role of mechanical stimulation. a, Creation of a mineralized matrix via osteogenic incubation of Osteoblasts and Osteocytes. **b**, Addition of osteoclast precursor cells to the mineralized model. **c**, Addition of breast cancer cells to the model. **d**, Mechanism of osteolytic metastatic response where presence of breast cancer cells growth factors that stimulate osteoclastogenesis through the RANKL/OPG pathway and downregulate osteoblastic activity. **e**, Mechanical compression leads to a reduction in the expression of these osteolytic growth factors by the breast cancer cells, which in turn leads to a reduction in expression of the factors supporting osteoclastogenesis, whereas osteoblast activity is upregulated.